Heel effect adaptive flat field correction of digital x-ray detectors

Yongjian Yu and Jue Wang

Articles you may be interested in

A beam hardening and dispersion correction for x-ray dark-field radiography
Med. Phys. **43**, 2774 (2016); 10.1118/1.4948671

A novel approach to background subtraction in contrast-enhanced dual-energy digital mammography with commercially available mammography devices: Polychromaticity correction
Med. Phys. **42**, 6641 (2015); 10.1118/1.4933199

A unified statistical framework for material decomposition using multienergy photon counting x-ray detectors
Med. Phys. **40**, 091913 (2013); 10.1118/1.4817521

Monte Carlo performance on the x-ray converter thickness in digital mammography using software breast models
Med. Phys. **39**, 6638 (2012); 10.1118/1.4757919

High resolution stationary digital breast tomosynthesis using distributed carbon nanotube x-ray source array
Med. Phys. **39**, 2090 (2012); 10.1118/1.3694667

Heel effect adaptive flat field correction of digital x-ray detectors

Yongjian Yu[a)]
X-ray Products, Varian Medical Systems Inc., Liverpool, New York 13088

Jue Wang[b)]
Department of Mathematics, Union College, Schenectady, New York 12308

Purpose: Anode heel effect renders large-scale background nonuniformities in digital radiographs. Conventional offset/gain calibration is performed at mono source-to-image distance (SID), and disregards the SID-dependent characteristic of heel effect. It results in a residual nonuniform background in the corrected radiographs when the SID settings for calibration and correction differ. In this work, the authors develop a robust and efficient computational method for digital x-ray detector gain correction adapted to SID-variant heel effect, without resorting to physical filters, phantoms, complicated heel effect models, or multiple-SID calibration and interpolation.

Methods: The authors present the Duo-SID projection correction method. In our approach, conventional offset/gain calibrations are performed only twice, at the minimum and maximum SIDs of the system in typical clinical use. A fast iterative separation algorithm is devised to extract the detector gain and basis heel patterns from the min/max SID calibrations. The resultant detector gain is independent of SID, while the basis heel patterns are parameterized by the min- and max-SID. The heel pattern at any SID is obtained from the min-SID basis heel pattern via projection imaging principles. The system gain desired at a specific acquisition SID is then constructed using the projected heel pattern and detector gain map.

Results: The method was evaluated for flat field and anatomical phantom image corrections. It demonstrated promising improvements over interpolation and conventional gain calibration/correction methods, lowering their correction errors by approximately 70% and 80%, respectively. The separation algorithm was able to extract the detector gain and heel patterns with less than 2% error, and the Duo-SID corrected images showed perceptually appealing uniform background across the detector.

Conclusions: The Duo-SID correction method has substantially improved on conventional offset/gain corrections for digital x-ray imaging in an SID-variant environment. The technique is relatively simple, and can be easily incorporated into multiple-point gain calibration/correction techniques. It offers a potentially valuable tool for preprocessing digital x-ray images to boost image quality of mammography, chest and cardiac radiography, as well as automated computer aided diagnostic radiology. © *2013 American Association of Physicists in Medicine.* [http://dx.doi.org/10.1118/1.4813303]

Key words: anode heel effect, digital x-ray detector, gain calibration, nonuniformity, source-to-image distance

1. INTRODUCTION

Digital flat panel technology has been extensively used in medical x-ray imaging such as chest radiography, digital subtraction angiography, cardiology and mammography. Compared to conventional image intensifier-based x-ray systems, flat panel-based systems offer a larger field of view, extended dynamic range, and pleasant patient accessibility. However, due to panel design and manufacture limitations, the detector pixel matrix is not spatially uniform. Moreover, the anode heel effect causes variations in the x-ray beam intensity across the detector surface. The combination of the large-scale heel variation and localized gain variability of the detector contributes to the complex spatial nonuniformities in digital radiographs. In clinical imaging applications, they appear as artifacts that interfere with correct diagnosis and assessment of

diseases. Therefore, each pixel of the detector matrix must be corrected using flat field calibration techniques.[1,2]

We give an overview of conventional flat field correction techniques for panel detector nonuniformity and relevant work on heel effect correction. To highlight the problem, we focus on a widely used gain calibration method called offset/gain calibration and a model based heel effect suppression in anatomical images.

The observed x-ray signal acquired using an x-ray electronic panel detector is given by

$$I(i, j) = G(i, j) \cdot I_c(i, j) + N(i, j), \quad i, j \in \Omega, \quad (1)$$

where $I(i, j)$ is the raw image density at pixel position (i, j). $G(i, j)$ is the system gain relative variation (or simply, system gain) encoding the stationary, nonuniform exposure response of the detector at pixel (i, j). $I_c(i, j)$ is the underlying correct

image. $N(i, j)$ denotes the dark current noise in the detector at acquisition. Ω is the discrete domain of image pixel positions.

The offset/gain calibration estimates $G(i, j)$ and the expected value of $N(i, j)$, then uses them to correct any raw image $I(i, j)$, yielding an estimation of $I_c(i, j)$ as follows:

$$\hat{I}_c(i, j) = \frac{I(i, j) - \bar{D}(i, j)}{\hat{G}(i, j)}, \tag{2}$$

where

$$\hat{G}(i, j) = \frac{\bar{F}(i, j) - \bar{D}(i, j)}{\langle \bar{F}(i, j) \rangle_\Omega - \langle \bar{D}(i, j) \rangle_\Omega}. \tag{3}$$

$\bar{F}(i, j)$ and $\bar{D}(i, j)$ are the means of P flat field images $\{F_k(i, j)\}_{k = 1, 2, \ldots, P}$ with the same exposure and Q dark current images $\{D_l(i, j)\}_{l = 1, 2, \ldots, Q}$, respectively. $\langle \cdot \rangle_\Omega$ denotes the pixel average over the active region Ω of the detector. $\bar{D}(i, j)$ is the offset that approximates the expectation of $N(i, j)$. $\hat{G}(i, j)$ is an approximation of $G(i, j)$ that contains random noise and measurement errors. If P and Q are sufficient large, $\hat{G}(i, j) \rightarrow G(i, j)$.

The conventional method for flat field calibration is performed at a fixed SID, usually the middle of the SID range in a clinical setting. The resulting gain factor is then applied to correct images acquired across a range of SIDs. The problem with this is that the heel effect and beam geometrical effects are SID-dependent. The more an acquisition SID differs from the calibration SID, the higher the residual field inhomogeneity in the corrected image. To alleviate this problem, it seems possible to use an empirical method, that is to calibrate the system at multiple SIDs with sufficiently small spacing, calculate an SID-dependent gain correction factor $\hat{G}(i, j; d)$ via linear interpolation, and apply $\hat{G}(i, j; d)$ to the images to be corrected. However, the digital receptors may also show nonlinear exposure response characteristics that require multiple-dose (or multiple-point) gain calibration.[2,3] An extended receptor calibration with multiple-dose (usually a dozen) and multiple-SID (half a dozen) would heavily burden the calibrators.

The flat field offset/gain calibration can be traced back to the era of film radiography. In Refs. 4 and 5, a digitized image of a "blank" film was used to correct field nonuniformity in mammograms. A computational method based on heel effect modeling and image partitioning was proposed in Ref. 6. Direct exposure areas in an uncorrected image were segmented out. The heel effect model fitting to the directly exposed data was determined by regression analysis. The fitting model was then used to correct the images. However, the model assumed a mono-energetic radiation source and ignored the beam hardening effects. Being a 1D model, it merely considered the cathode-anode directional field variations. Moreover, the method demanded that the direct exposure regions to be sufficiently large and distributed across the image domain for reliable estimation of the model parameters. The method was tested in correcting images of extremity examinations, but had limited applications in chest radiographs since they rarely contain direct radiation regions. This heel effect model[6] was generalized to a 2D model with a continuous spectral beam taken into account.[7] The structural and material information about the anode were regarded as known parameters and used in the model formula to generate a simulated heel pattern. The simulated heel pattern was then registered to the uncorrected images to correct the field nonuniformity. This analytical model was still oversimplified, lacked sufficient accuracy and detailed information regarding x-ray tube design and manufacturing. Furthermore, it did not address how image registration based on empirical heel distributions could be utilized in general radiography.

The physical beam filter was introduced to compensate for the heel effect in mammograms.[8] Each x-ray tube needed a specifically designed filter that was coupled to the x-ray tube window in use. Later in Ref. 9, a bowl phantom calibration approach was developed for correcting digitized mammograms. During calibration the phantom was placed closely under the x-ray tube. A correction matrix was obtained from the phantom images. The matrix was then applied to correct field inhomogeneity in mammogram during image acquisition. The beam path obliquity effects within the soft tissue were corrected computationally. Neither technique is truly effective in correcting localized, correlated noises resulting from x-ray receptors in digital imaging systems. Aside from mammography, many examinations in general radiography use much wider ranges of tube kVp and SID settings as well as a much larger field of view, causing highly versatile heel effects. This makes it necessary to employ many specifically designed Perspex filters or phantoms based on the examination type. Therefore, the beam filtering and phantom calibration techniques seem inadequate and impractical for nonhomogeneity correction in digital radiography.

The residual inhomogeneity exists in the corrected digital radiographs caused by SID mismatch during calibration and correction. It may hinder correct attenuation measurements of tissue from the imaged anatomy. In this work, we present a Duo-SID projection model which improves on the mono-SID scheme. With minimal additional effort, the proposed Duo-SID correction technique promises to overcome the excessive calibration burden and other limitations associated with empirical multi-SID-interpolation correction. The paper is organized as follows. In Sec. 2, we describe the method for separating detector gain and basis heel effect, introduce the projection model, and derive a relationship between the spatially discretized heel effects at different SIDs. In Sec. 3, we test and validate the method using real and simulated data and a commercial panel. Potential issues in application of the method are discussed in Sec. 4, and conclusions are drawn in Sec. 5.

2. MODELS AND METHODS

2.A. System nonuniformity model

The radiographic imaging system setup and coordinates are illustrated in Fig. 1. The beam axis is assumed to be normal to the detector surface. The xy-plane lies on the surface of the detector with the origin at the projection of the focal spot on the detector surface. The x-axis is the anode–cathode axis. The z-axis is along the beam axis pointing to the detector. The anode patch being bombarded by electrons is inclined by a small angle (termed anode angle) θ ($7° \leq \theta \leq 15°$) relative to
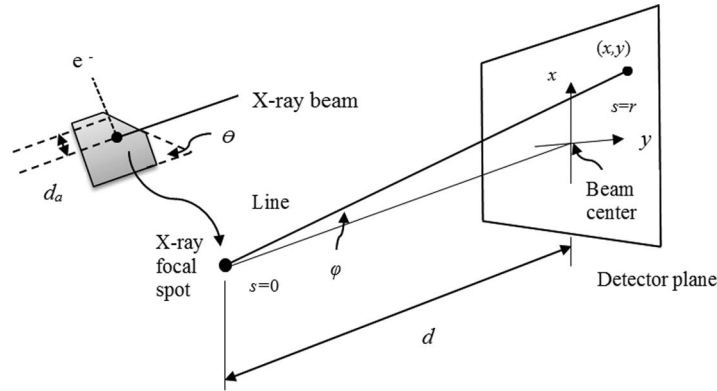
FIG. 1. X-ray imaging geometry and anode structure.

the z-axis. Its normal is parallel to the x-axis, with an average beam penetration depth in the anode d_a. The tangent plane of the focal spot is parallel to the y-axis.

The basic projection imaging equation is

$$I(x, y, d) = \int_0^{E_{\max}} S_0(E')E'$$
$$\times \exp\left\{-\int_0^{r(x,y)} \mu(s; E', x, y)\,ds\right\}dE'. \quad (4)$$

$S_0(E)$ is the photon fluence spectrum composed of the Bremsstrahlung spectrum and characteristic lines emitted by the anode target. E is the photon energy and $E_{\max}$ is the cut-off photon energy. $r(x, y)$ is the path of a ray. $\mu(s; E, x, y)$ is the linear attenuation coefficient along the ray path. Taking into account the beam divergence and obliquity, we obtain the point-source beam incident fluence on the detector surface

$$I(x, y; d)$$
$$= \frac{1}{4\pi d^2} \cos^3\varphi \int_0^{E_{\max}} S_0(E')E'$$
$$\times \exp\left\{-\mu_T(E')d_a \frac{\sqrt{1 + (x/d)^2}}{\tan\theta + x/d} - \frac{\mu_C(E')L}{\cos\varphi}\right\}dE', \quad (5)$$

where φ is the angle between the beam axis z and a ray that hits the detector surface at point (x, y). The $\cos^3\varphi$ term governs the x-ray beam divergence effects according to the inverse square law and obliquity.[10] μ_T and μ_C are the linear attenuation coefficients of the target and aluminum, respectively. L is the thickness of the aluminum (Al) equivalent filter composing the x-ray tube window and the added calibration filter. From Eq. (5), by way of ray tracing, the far-field radiation fields at two distinct distances d and d' ($d' > d$ and $d \gg$ distance of added filter to source) satisfy the projection relationship

$$I(x, y; d') = \frac{1}{m^2} I\left(\frac{x}{m}, \frac{y}{m}, d\right), \quad (6)$$

where $m = d'/d$ is the magnification factor.

Raw digital radiographic images suffer from high-frequency, correlated artifacts caused by nonuniform response characteristics across the detector pixel matrix, and low frequency background artifacts resulted from the x-ray beam nonuniformity. The two deterministic artifacts are jointly modeled by the system gain $G(i, j; d)$, which can be expressed as a product of the two factors

$$G(i, j; d) = g_0(i, j) \cdot \tilde{g}(i, j; d), \quad (7)$$

where $g_0(i, j)$ is the detector nonuniformity gain factor, independent of SID, and $\tilde{g}(i, j; d)$ is the sampled beam nonuniformity at pixel site (i, j). In conventional correction methods, $\tilde{g}(i, j; d)$ is regarded as independent of d and thus absorbed into the detector gain.

The presampled field nonuniformity $g(x, y; d)$ is caused by the inhomogeneous incident fluence $I(x, y; d)$ in Eq. (5), normalized to unity,

$$g(x, y; d) = \frac{I(x, y; d)}{\langle I(x, y; d)\rangle_S}, \quad (8)$$

where S is the continuous domain corresponding to the active region of the detector in (x, y) coordinates. The sampled beam pattern is the detector pixel sampling of the presampled pattern

$$\tilde{g}(i, j; d) = g(x, y; d) * s(x - x_i, y - y_j),$$
$$x_i = -c_x + ih,$$
$$y_j = -c_y + jh. \quad (9.1)$$

$s(x, y) = \frac{1}{h^2} \text{rect}\left(\frac{x}{h}\right)\text{rect}\left(\frac{y}{h}\right)$ is the detector pixel averaging filter. h is the pixel spacing. (c_x, c_y) are the coordinates of the beam center (or focal spot projection position) in the image plane with respect to the detector reference frame where the origin is the upper left corner of the receptor. Since the beam field inhomogeneity is slowly varying relative to h, we approximate $s(x, y)$ with an impulse function $\delta(x, y)$. Equation (9.1) becomes

$$\tilde{g}(i, j; d) \approx g(x_i, y_i; d). \quad (9.2)$$

Figure 2 shows the typical contour plots of $g(x, y; d)$ at SID = (43, 53, 63 in.). These values were taken to match those for the experiments in Sec. 3. They reflect approximately the typical settings in clinical projection imaging. In clinics, the SID is commonly set between 39 and 72 in. For portable exams, the SID of less than 39 in. is also used, but
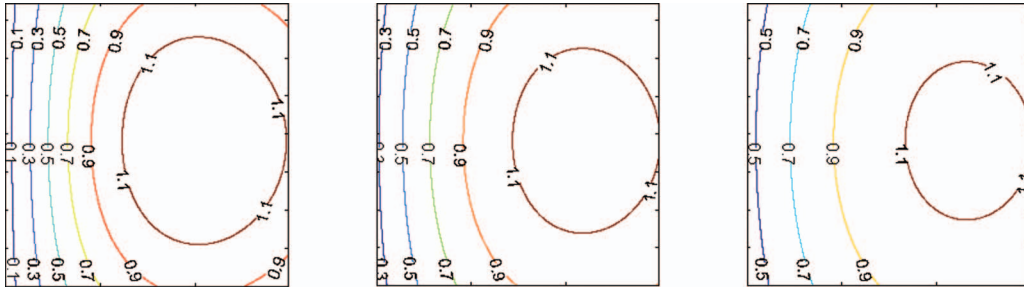
FIG. 2. Beam nonuniformity shown as contours of equal values at SID = (43, 53, 63 in.) from left to right. The system modeling parameter setup is described in Sec. 3.B. The coordinate origin is at the bottom left corner for these plots.

nowhere near the frequency of SID greater than 39. We observe that the variations in $g(x, y; d)$ are more pronounced at smaller d. From Fig. 2 or Eq. (5), it is expected that the heel effect will be flattened as d gets larger (relative to the dimension of the detector), and eventually $g(x, y; d) \approx 1$. If the gain calibration performed at SID = d is applied to an uncorrected image acquired at a SID = d', the corrected image will retain inevitably a residual nonuniformity that equals the ratio $\tilde{g}(i, j; d)/\tilde{g}(i, j; d')$. See Fig. 4 for an example and Appendix A for derivation.

2.B. Duo-SID projection model

We derive a model for projecting the basis beam pattern on the minimum SID plane to a higher SID setting. Then a method is devised for extracting the detector gain and basis beam pattern from gain calibrations at min/max SID settings. The system gain at any given SID setting can be constructed via projection and recombination.

2.B.1. Projection of basis beam model

The forward projection of the basis beam pattern $g(x, y; d_{\min})$ onto a farther plane at d can be derived from Eqs. (6) and (8),

$$g(x, y; d) = \frac{g\left(\frac{x}{m}, \frac{y}{m}; d_{\min}\right)}{\left\langle g\left(\frac{x}{m}, \frac{y}{m}; d_{\min}\right)\right\rangle_S}, \quad \forall (x, y) \in S, \quad (10)$$

where $m = d/d_{\min}$ is the projection magnification factor. This relationship relates the beam nonuniformities on two different planes normal to the beam central axis. The right hand side of Eq. (10) is interpreted as a magnified version of $g(x, y; d_{\min})$ cropped to fit the domain S, and then renormalized to unity over S. In the digital domain, the projection relation becomes

$$\tilde{g}(i, j; d) = \frac{g\left(\frac{x_i}{m}, \frac{y_j}{m}; d_{\min}\right)}{\left\langle g\left(\frac{x_i}{m}, \frac{y_j}{m}; d_{\min}\right)\right\rangle_\Omega}. \quad (11)$$

$g(\frac{x_i}{m}, \frac{y_j}{m}; d_{\min})$ is the reconstructed, magnified beam pattern

$$g\left(\frac{x}{m}, \frac{y}{m}; d_{\min}\right) = \sum_{(i,j)\in\Omega} \tilde{g}(i, j; d_{\min}) \operatorname{sinc}\left(\frac{\frac{x}{m} - x_i}{h}\right)$$

$$\times \operatorname{sinc}\left(\frac{\frac{y}{m} - y_j}{h}\right). \quad (12)$$

The derivation is provided in Appendix B. For convenience, we adopt a projection operator for the relevant computing process,

$$\tilde{g}(i, j; d) = P\left\{\tilde{g}(:, :, d_{\min}); h, (c_x, c_y), (i, j), (d_{\min}, d)\right\}. \quad (13)$$

$P\{\cdot\}$ implements a series of processing: (1) reconstruct the presampled beam pattern from the sampled array $\tilde{g}(:, :, d_{\min})$ in the beam center coordinate system, (2) magnify the reconstruction by a factor $m = d/d_{\min}$, (3) sample at the position corresponding to the detector pixel site (i, j), and (4) normalize over domain Ω.

2.B.2. Extraction of basis beam pattern and detector gain

Combining the min/max SID calibrated gains [obtained from Eq. (3)] and Eq. (7), we obtain two approximate equations

$$\hat{G}(i, j; d_{\min}) \approx g_0(i, j) \cdot \tilde{g}(i, j; d_{\min}), \quad (14.1)$$

$$\hat{G}(i, j; d_{\max}) \approx g_0(i, j) \cdot \tilde{g}(i, j; d_{\max}). \quad (14.2)$$

The approximation is caused by using finite number of flat field images to estimate $G(i, j; d)$. To solve for $g_0(i, j)$, $\tilde{g}(i, j; d_{\min})$ and $\tilde{g}(i, j; d_{\max})$, another independent equation is needed. From Eq. (11), the projection relation gives

$$\tilde{g}(i, j; d_{\max}) = \frac{g\left(\frac{x_i}{M}, \frac{y_j}{M}; d_{\min}\right)}{\left\langle g\left(\frac{x_i}{M}, \frac{y_j}{M}; d_{\min}\right)\right\rangle_\Omega}, \quad (14.3)$$

where $M = d_{\max}/d_{\min}$. We seek an iterative solution of problem (14.1–3). Since the basis beam pattern $\tilde{g}(i, j; d_{\max})$ varies more slowly than $\tilde{g}(i, j; d_{\min})$, we set an initial guess $\tilde{g}^{(0)}(i, j; d_{\max}) = 1$. At the kth step, the detector gain and beam patterns at min/max SID are computed as follows:

$$g_0^{(k)}(i, j) = \frac{\hat{G}(i, j; d_{\max})}{\tilde{g}^{(k)}(i, j; d_{\max})}, \quad (15.1)$$

$$\tilde{g}^{(k)}(i, j; d_{\min}) = \frac{\hat{G}(i, j; d_{\min})}{g_0^{(k)}(i, j)} * h_\sigma(i, j), \quad (15.2)$$

$$\tilde{g}^{(k+1)}(i, j; d_{\max}) = P\{\tilde{g}^{(k)}(:, :, d_{\min}); h, (c_x, c_y), (i, j),$$

$$\times (d_{\min}, d_{\max})\}. \quad (15.3)$$

$h_\sigma(i, j)$ is a discrete 2D Gaussian filter with standard deviation σ and $*$ denotes convolution. This low-pass filter is applied to prevent the random noise in the calibrated $\hat{G}(i, j; d_{\min})$ and $\hat{G}(i, j; d_{\max})$ from propagation and being amplified through the iterative projection.

2.B.3. System gain at any SID

With the estimates of detector gain $\hat{g}_0(i, j)$ and beam nonuniformity $\hat{\tilde{g}}(i, j; d_{\min})$, we can construct the system gain at any SID setting within the range $[d_{\min}, d_{\max}]$,

$$\hat{G}(i, j; d) = \hat{g}_0(i, j) \frac{\hat{g}\left(\frac{x_i}{m}, \frac{y_j}{m}; d_{\min}\right)}{\left\langle \hat{g}\left(\frac{x_i}{m}, \frac{y_j}{m}; d_{\min}\right)\right\rangle_\Omega}. \quad (16)$$

Finally, the raw image $I(x, y)$ acquired at any SID can be corrected using Eq. (2).

2.C. Algorithm summary

The two core algorithms for implementing our method, the Duo-SID projection correction, are summarized as follows.

2.C.1. Separation algorithm

$[\tilde{g}(:, :, d_{\min}), \tilde{g}(:, :, d_{\max}), g_0(:, :)] \leftarrow$ separator$\{\hat{G}(:, :, d_{\min}), \hat{G}(:, :, d_{\max}),$ $d_{\min}, d_{\max}\}$

Initialize: $k \leftarrow 0$, $\tilde{g}^{(0)}(d_{\max}) \leftarrow 1$
Do
 Compute $\tilde{g}(d_{\min})$:
  $g_0^{(k)} \leftarrow \dfrac{\hat{G}(d_{\max})}{\tilde{g}^{(k)}(d_{\max})}$
  (Optionally, detect and correct defective pixels in $g_0^{(k)}$)
  $\tilde{g}^{(k)}(d_{\min}) \leftarrow \dfrac{\hat{G}(d_{\min})}{g_0^{(k)}}$
  $\tilde{g}^{(k)}(d_{\min}) \leftarrow$ imfilter $\left\{\tilde{g}^{(k)}(d_{\min})\right\}$
 Update $\tilde{g}(d_{\max})$:
  $\tilde{g}^{(k+1)}(d_{\max}) \leftarrow$ projector $\left\{\tilde{g}^{(k)}(d_{\min}); h, (c_x, c_y), (i, j), (d_{\min}, d_{\max})\right\}$
  $k \leftarrow k + 1$
while $\| \tilde{g}^{(k+1)}(d_{\max}) - \tilde{g}^{(k)}(d_{\max}) \| > \epsilon$ or $k <$ maxiter

---

The optional step deals with possible defective pixels that could lead to division by zero.

2.C.2. Projection algorithm

$\tilde{g}(:, :, d) \leftarrow$ projector $\left\{\tilde{g}(:, :, d_{\min}); h, (c_x, c_y), (:, :), (d_{\min}, d)\right\}$

$m \leftarrow \dfrac{d}{d_{\min}}$
$\tilde{g} \leftarrow$ imresize$\{\tilde{g}(d_{\min}), m\}$
$b \leftarrow (m - 1) \times (c_x, c_y)$
$\bar{b} \leftarrow$ round $\left(\frac{b}{h}\right)$
$\tilde{g} \leftarrow$ imcrop$\{\tilde{g}, [\bar{b}, \text{imsize}\{\text{detector}\}]\}$
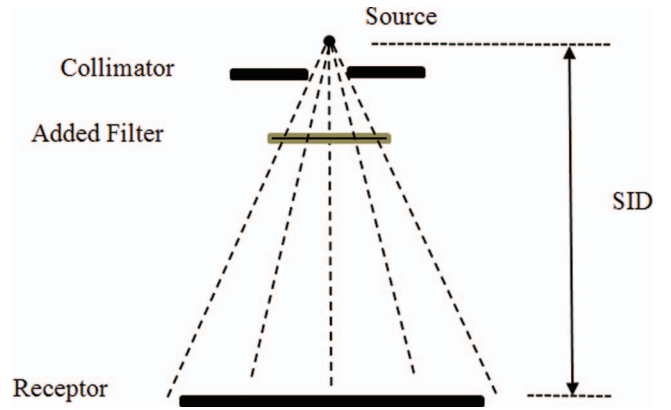$\tilde{g}(d) \leftarrow \dfrac{\tilde{g}}{\text{median}\{\tilde{g}\}}$

FIG. 3. Beam-imager geometry for calibration.

Imresize$\{A, m\}$ returns an image that is m times of the size of A. Imcrop$\{B, rect\}$ returns a portion of B in the region $rect$. Round(x) rounds the number x to the nearest integer. $[\bar{b}, \text{imsize}]$ specifies a rectangle region within the detector matrix. $\bar{b}$ is the vector representation of the row and column indices of the upper left corner of the region occupied by the detector. The geometrical relation is illustrated in Appendix C.

3. EXPERIMENTS AND RESULTS

3.A. System setup and general test

The beam geometry and experiment setup for calibration and correction are illustrated in Fig. 3. The imaging system used a Sedecal SHF-65 generator with a Varian G292 tube and a Varian 4343 CB dynamic panel. For all data acquisition the x-ray tube peak kilo-voltage was fixed at 72 kV. The added filter with 0.5 mm Cu plus 2 mm aluminum was used to harden the beam to RQA-5 quality. The half value layer (HVL) of 6.8 mm Al was measured. The beam was collimated with about 1 in. margin. Table I lists the exposure settings used to acquire flat field images for calibration, flat field, and hand phantom images for correction. F_{1-10} stands for flat field images numbered 1 to 10. Ten dark current images were acquired prior to exposure data acquisitions. The offset was computed as frame average of the ten dark current images. The receptor is in 2×2 binning mode, and the image pixel dimensions are 1488×1488, with a bit-depth of 16. The 2×2 binned pixel pitch is 0.278 mm.

$\hat{G}(:, :, 43'')$ and $\hat{G}(:, :, 63'')$ were calculated using the ten flat field images exposed at 4 mAs with 43″ SID and 8 mAs with 63″ SID, respectively, shown in Fig. 4. Notice the gain nonuniformities and heel effect. These two system gains were input to the Duo-SID correction. The geometrical parameters

TABLE I. Flat field (F) and hand phantom (H) images acquired at the same kVp = 72 kV.

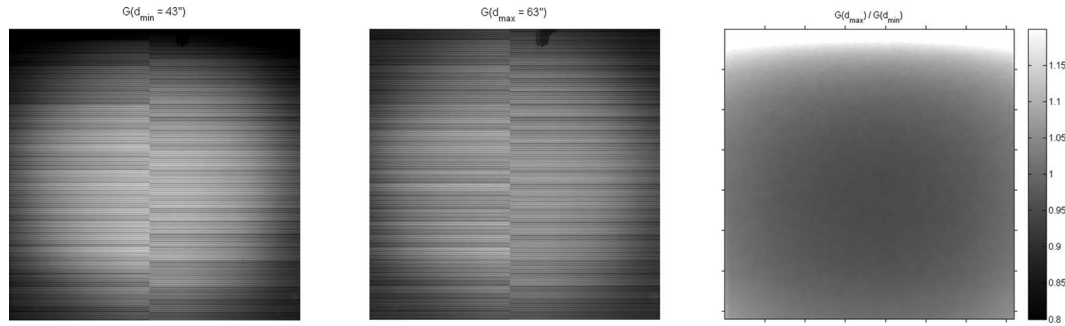| SID	Calibration		Correction
43″	4 mAs F_{1-10}	Min-SID calibration	
53″	8 mAs F_{1-10}	Ground truth	4 mAs F_{1-5} and H_{1-5}
63″	8 mAs F_{1-10}	Max-SID calibration	

FIG. 4. Left and middle: Min/max SID system gains from conventional offset/gain calibration at SID = 43″ and 63″. Right: Residual nonuniformity resulted from applying gain calibrated at d_{max} to correction at d_{min}. Variations of greater than 20% were observed.

are known *a priori*: $d_{min} = 43''$, $d_{max} = 63''$, $h = 0.278$ mm, $(c_x, c_y) = (245.94, 210.51)$ mm. The algorithmic parameters are set empirically: $\sigma = 60$, $\epsilon = 1.5$, maxiter = 10. The extracted beam patterns and detector gain are shown in Fig. 5. The algorithm converged in six iterations.

We performed three evaluations to assess the Duo-SID algorithm against the linear interpolation, the conventional (mono-SID) method, and the exact calibration calculated as the ground truth gain.

3.A.1. Gain evaluation

The ground truth gain $\hat{G}(53''; \text{exact})$ was obtained using the ten flat field images exposed at 8 mAs with 53″ SID. We computed $\hat{G}(53''; \text{Duo-SID})$ using Eq. (16) with the extracted detector gain and beam pattern at min-SID. The linear interpolated gain is $\hat{G}(53''; \text{interpolation}) = \frac{1}{2}[\hat{G}(43''; \text{exact}) + \hat{G}(63''; \text{exact})]$, and the conventional or mono-SID gain is $\hat{G}(53''; \text{conventional}) = \hat{G}(63''; \text{exact})$.

We use the root mean square error (RMSE) to measure the fidelity of the gains computed by the three methods relative to the ground truth gain. The results are listed in Table II. A smaller RMSE value indicates a better performance. The Duo-SID correction method gives the best system gain among the three methods.

3.A.2. Flat field image correction

Five flat field images acquired at 4 mAs with 53″ SID were used for the nonuniformity correction. We applied the system gains obtained from the Duo-SID, linear interpolation, con-

ventional method, and exact calibration to the offset-corrected flat field images. The RMSE of each corrected image against its ground truth image was calculated. The RMSEs of all five images were then averaged.

In addition to RMSE, we use the variation factor[2] (VF) to quantify the flatness of the corrected flat field images. We select a set of regions of 32×32 pixels uniformly distributed across the image, and calculate the mean values from all regions. The VF is the standard deviation over the average of all mean values. A smaller VF indicates a better correction. The results of RMSE and VF are listed in Table II. The Duo-SID correction gives the best result and is the closest to the ground truth gain correction.

Lastly, we compare column and row-directional 1D profiles of the corrected images along the lines intersecting at the focal spot projection position: round$\{(c_x, c_y)/h\} = (885, 757)$, obtained experimentally. The 1D profiles along the lines with fixed row index = 757 and column index = 885 were smoothed using an average filter with an 81×81 pixel window. The profiles are plotted in Fig. 6. The RMSE measurements are given in Table II. The Duo-SID profiles are flatter and show less variation than those from interpolation and conventional methods.

3.A.3. Hand phantom image correction

Five hand phantom images acquired at 4 mAs with 53″ SID were corrected using the three methods and exact gain calibration. The RMSEs from the five images were averaged for each method and listed in the last column of Table II.
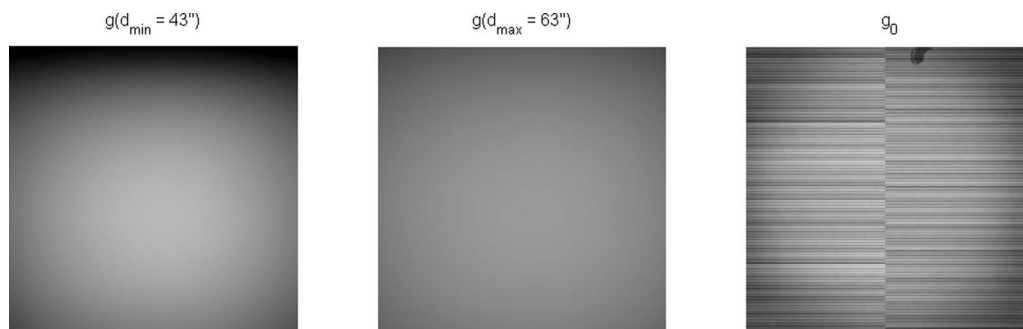

FIG. 5. Extracted beam patterns at min/max SIDs and detector gain map.

TABLE II. Quantification of the Duo-SID and alternative correction methods at SID = 53″.

Method	$\hat{G}(53'')$ RMSE	Correction of flat field image RMSE	VF	$1D_x$	$1D_y$	Hand image RMSE
Exact	…	…	0.0004	…	…	…
Duo-SID	0.004	73.87	0.0043	16.78	62.46	74.05
Interpolation	0.012	241.24	0.0144	84.91	159.91	241.66
Conventional	0.020	350.65	0.0215	195.85	288.79	349.54

A comparison of the offset-only corrected and Duo-SID corrected hand images is shown in Fig. 7. The latter shows appealing uniform background across the detector.

In all three evaluations, the Duo-SID correction method demonstrates the best performance. It decreases the RMSEs of corrected images by approximately 70% compared to interpolation, and about 80% compared to the conventional method.

3.B. Validation of separation algorithm

We tested the separation algorithm using simulated heel effects and real detector gain. With the typical detector calibration setup as in Fig. 3, we simulated the beam patterns at SID = 43″ and 63″ using Eqs. (5) and (8). The x-ray source was simplified to emit the Bremsstrahlung spectral beam with a tungsten target and a tube peak voltage of 72 kV. Thus, according to the Kramers formula, $S_0(E) = CZ(E_{max} - E)\frac{v_0}{c^2}$, where $E_{max} = 72$ keV, Z is the tungsten anode atomic number, $Z = 74$, v_0 is the electron initial velocity, C is a material-dependent constant, and c is the speed of light. Other simulation parameters are 12° anode angle and 21 mm Al added filtration. The energy-dependent mass attenuation coefficients of the aluminum and tungsten target are taken from Refs. 11 and 12. The cathode-anode axis is the x axis. The beam center is $(20, -30)$ pixels off the image center. The average electron penetration depth $d_a = 0.02$ mm.

We simulated the min/max SID system gains by multiplying the corresponding simulated beam patterns with the real detector gain extracted in Sec. 3.A (see Fig. 5). The simulated

system gains are shown in Fig. 8. Finally, we applied the Duo-SID separation algorithm to extract the beam inhomogeneity fields and detector gain. The results are displayed in Fig. 9. They match their ground-truth data visually. The corresponding contour plots of the ground truth beam patterns are shown earlier in Fig. 2. The RMSEs of the extracted beam nonuniformity at SID = 43″ and 63″, and extracted detector gain are 0.0116, 0.0116, and 0.0121, respectively. This test demonstrates the efficacy of the separation algorithm with known ground truth heel effect and detector gain data.

4. DISCUSSION

Several points need to be considered to facilitate practical implementation of the proposed method. For optimal diagnostic imaging, the imager is set up and calibrated such that the beam axis passes through the center of the image receptor. This geometry condition, however, might be impractical to maintain in use. Transverse and longitudinal alignment errors could occur after SID resetting. The misalignment of the two centers can be detected and monitored routinely by analyzing flat field images acquired under the condition of lower kVp. The peak and approximate circular symmetry of the beam geometric distortion in lower kVp flat field images serve as image features for detection of the focal spot projection in the imager. As long as the transverse misalignment between the beam center and detector center is small, the method can automatically compensate for the misalignment. However, if the misalignment exceeds some preset limit, the realignment or system setup calibration should be performed manually.

In cases where the detector (such as a portable type) is rotated 90°, 180°, or 270° from the calibration orientation, system recalibration may be unnecessary. The existing calibration files can be used through rotational alignment. The rotation angle can be determined by exploiting the empirical, characteristic distributions of the heel pattern intensity profiles.

We acknowledge that the tube kVp settings and receptor nonlinearity can influence the calibration. The calibration is valid, strictly speaking, for a fixed kVp setting and within the linear sensitivity range of the detector. The anode heel effect
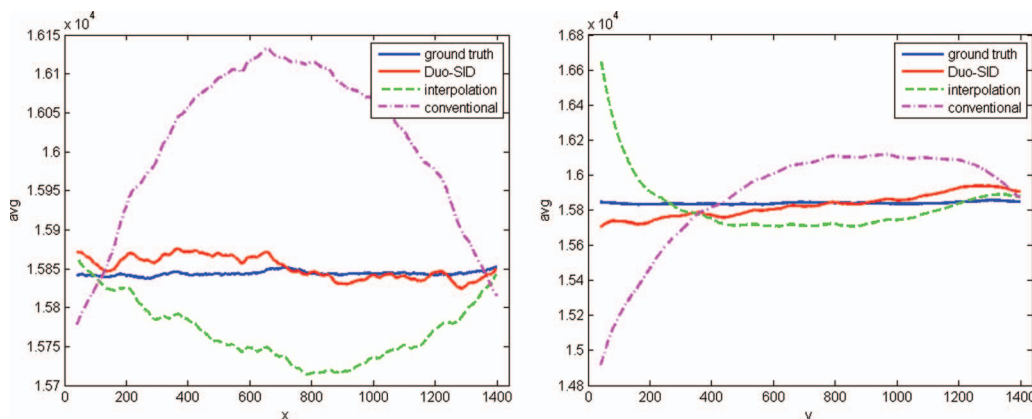

FIG. 6. 1D intensity profiles at $y = 757$ (left) and $x = 885$ (right) smoothed using an average filter with an 81×81 pixel window in the corrected flat field image at SID = 53″.
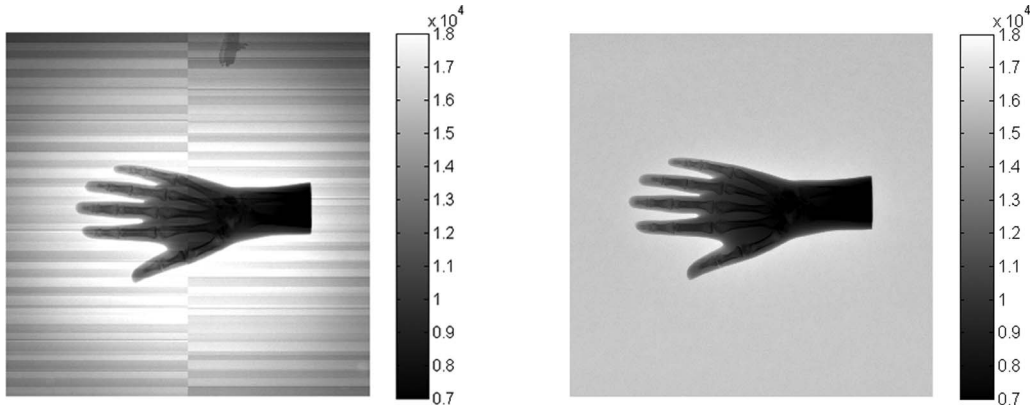
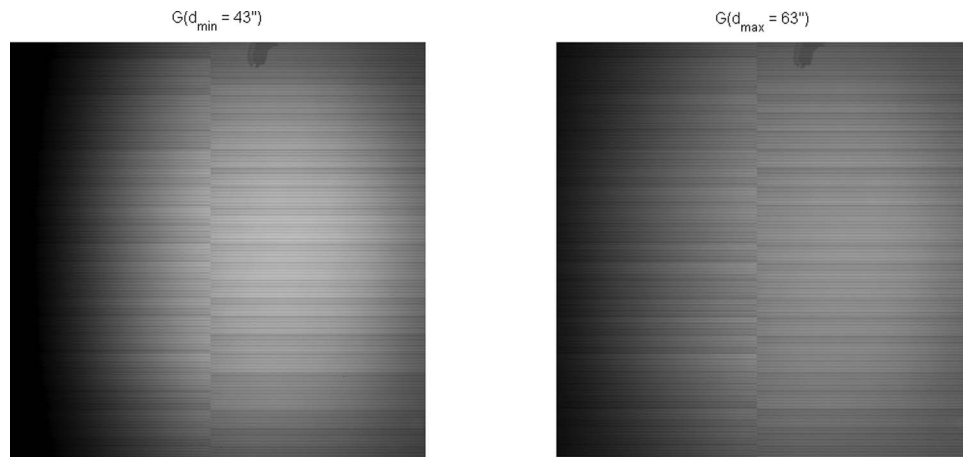FIG. 7. Offset corrected (left) and Duo-SID corrected (right) hand images at SID = 53″.

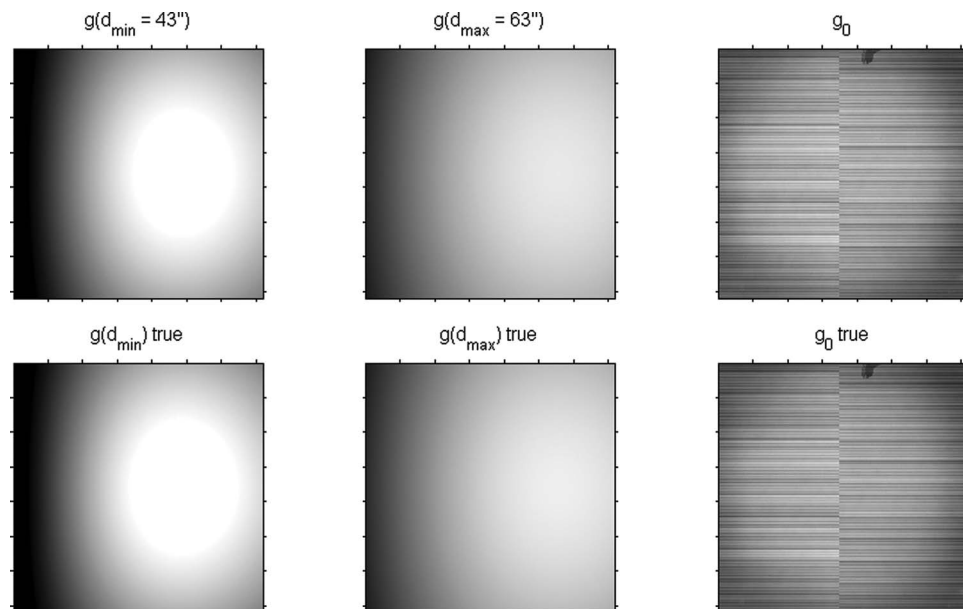FIG. 8. Simulated system gains at min-SID = 43″ and max-SID = 63″.

FIG. 9. Top: Simulated field inhomogeneity and detector gain extracted using the Duo-SID separation algorithm. Bottom: The corresponding ground truth data.

increases with the increase of kVp, and the receptor responds nonlinearly to high dose levels. If a calibration is made at a very low kVp, the anode heel effects might be neglected. On the other hand, if too high a dose is used, the calibration gain would suffer from saturation effects. In either case, the calibration would fail to correct images acquired under the most commonly used clinical settings.

Lastly, we outline a scheme for generalizing our method to address variable kVp and detector nonlinearity for general radiography examinations, where the kVp may be set over a wide range of 40–120 kV. During calibration, the kVp is set at three potentials: 50, 70, and 90 kV. At each setting, the detector system is calibrated using the Duo-SID method at moderate, intermediately high, and high dose levels independently, resulting in three sets of gain and basis heel pattern files for each kVp setting. The tri-dose gains corresponding to 70 kVp are fitted to a second-order polynomial gain as a function of dose, representing the nonlinear gain. The three min (or max) heel patterns corresponding to each kVp are averaged. The three averaged min (or max) heel patterns are then fitted to a second-order polynomial min (or max) heel pattern as a function of kVp. During correction, a newly acquired image (at certain acquisition kVp and SID) can be corrected using our method with the polynomial fitted gain and basis heel patterns.

5. CONCLUSIONS

We have derived a Duo-SID correction method to enhance the conventional offset/gain flat field correction for digital x-ray imaging in a varying SID environment. This method directly analyzes system gains calibrated at the admissible minimum and maximum SIDs, resulting in an SID-invariant detector gain. An optimal system gain is predicted at any SID by combining the detector gain and heel effect obtained using the projection imaging principles. The proposed method is characterized by its purely computational nature in the sense that it requires no physical filters or phantoms. Other advantages include: (1) the procedure is relatively simple, and does not involve any complicated models of the heel effect or model parameter tuning, (2) with relatively minor efforts the proposed method can be incorporated into multiple-point gain calibration/correction techniques, and (3) compared to the empirical interpolation method that demands densely spaced SID calibrations, our method is based on the optical projection imaging. The Duo-SID gain calibration technique has demonstrated promising performance. It offers a potentially valuable tool for preprocessing digital x-ray images for improved mammography, chest and cardiac radiography, as well as automated computer aided diagnostic radiology.

APPENDIX A: MISMATCH SID RESIDUAL INHOMOGENEITY

According to Eq. (1), the observed, uncorrected image acquired at SID = d is related to its underlying correct image $I_c(i, j)$ by

$$I(i, j) = G(i, j; d) \cdot I_c(i, j) + N(i, j).$$

If the gain is calibrated at the same SID, a perfectly corrected image would result from Eq. (2), ignoring the random noise,

$$I_c(i, j) = \frac{I(i, j) - \bar{D}(i, j)}{G(i, j; d)}. \tag{A1}$$

On the other hand, if the gain calibration is made at a different SID = d', an imperfectly corrected image would be obtained,

$$I_c'(i, j) = \frac{I(i, j) - \bar{D}(i, j)}{G(i, j; d')}. \tag{A2}$$

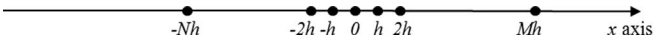Taking the ratio of Eqs. (A2) and (A1), using Eq. (7) and neglecting random scatter, we have

$$I_c'(i, j) = I_c(i, j) \frac{G(i, j; d)}{G(i, j; d')} = I_c(i, j) \frac{\tilde{g}(i, j; d)}{\tilde{g}(i, j; d')}.$$

The SID mismatch between calibration and correction causes the corrected image residual heel effect inhomogeneity by a factor of $\tilde{g}(i, j; d)/\tilde{g}(i, j; d')$.

APPENDIX B: DERIVATION OF EQ. (12)

Consider a one dimensional signal $f(x)$. It can be obtained by interpolating among the samples $\{ f(ih), i = \dots, -2, -1, 0, 1, 2, \dots \}$ with sample period h. Using the Wittaker-Shannon interpolation formula, an ideal reconstruction is given by

$$f(x) = \sum_{i=-N}^{M} f(ih) \cdot \text{sinc}\left(\frac{x - ih}{h}\right). \tag{B1}$$
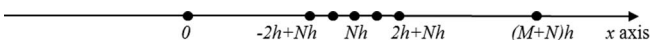

The formula is a convolution expressed as a weighted sum of scaled instances of the reconstruction filter centered at the sample points.

Let $i = j - N$. Equation (B1) can be written as

$$f(x) = \sum_{j=0}^{M+N} f(jh - Nh) \cdot \text{sinc}\left(\frac{x - jh + Nh}{h}\right)$$

$$= \sum_{j=0}^{M+N} \tilde{f}(jh) \cdot \text{sinc}\left(\frac{x - jh + Nh}{h}\right), \tag{B2}$$

where $\tilde{f}(jh)$ is expressed in the detector image domain.

Substituting x in (B2) with x/m yields

$$f\left(\frac{x}{m}\right) = \sum_{j=0}^{M+N} \tilde{f}(jh) \cdot \text{sinc}\left(\frac{\frac{x}{m} - jh + Nh}{h}\right). \qquad \square$$

APPENDIX C: POSITION OF DETECTOR REGION IN THE REFERENCE FRAME OF MAGNIFIED DETECTOR AREA

The figure illustrates the geometrical relation of two reference frames. The small box inside shows the detector area. The large box outside shows the magnified detector area. The

beam center in the detector reference frame is at (c_x, c_y). The beam center could be misaligned with the image center which is at the center of the detector area by an offset.
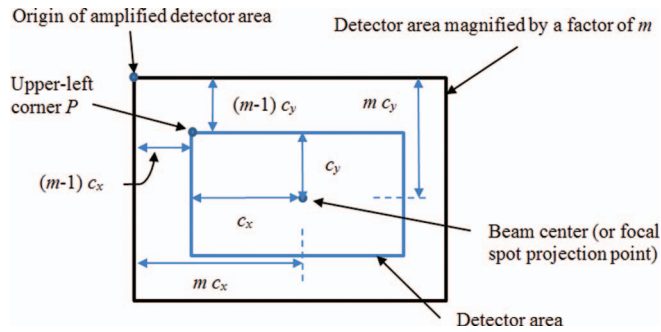
After magnification about the beam axis by a factor m, the detector becomes m^2 larger in area. The new coordinates of the beam center in the magnified detector reference frame are (mc_x, mc_y). Thus, the coordinates of the upper left corner P of the detector area are $((m-1)c_x, (m-1)c_y)$.

[a)]Electronic mail: yongjian.yu@varian.com
[b)]Electronic mail: wangj@union.edu

[1]J. Seibert, J. Boone, and K. Lindfors, "Flat-field correction technique for digital detectors," Proc. SPIE **3336**, 348–354 (1998).
[2]A. Kwan, A. Seibert, and J. Boone, "An improved method for flat-field correction of flat panel x-ray detector," Med. Phys. **33**, 391–393 (2006).
[3]C. Schmidgunst, D. Ritter, and E. Lang, "Calibration model of a dual gain flat panel detector for 2d and 3d x-ray imaging," Med. Phys. **34**, 3649–3664 (2007).
[4]R. Highnam, M. Brady, and B. Shepstone, "A representation for mammographic image processing," Med. Image Anal. **1**, 1–18 (1996).
[5]J. Smith, S. Astley, J. Graham, and A. Hufton, "The calibration of grey levels in mammograms," *Proceedings of the 3rd International Workshop on Digital Mammography*, edited by K. Doi, M. L. Giger, R. M. Nishikawa, and R. A. Schmidt (Elsevier, New York, NY, 1996), pp. 195–200.
[6]G. Behiels, F. Maes, D. Vandermeulen, and P. Suetens, "Retrospective correction of the heel effect in hand radiographs," Med. Image Anal. **6**, 183–190 (2002).
[7]M. do Nascimento, A. Frère, and F. Germano, "An automatic correction method for heel effect in digitized mammography images," J. Digit. Imaging **21**, 177–187 (2008).
[8]A. Cowen, D. Brettle, and A. Workman, "Technical note: Compensation for field non-uniformity on a mammographic x-ray unit," Br. J. Radiol. **66**, 150–154 (1993).
[9]O. Pawluczyk and M. Yaffe, "Field nonuniformity correction for quantitative analysis of digitized mammograms," Med. Phys. **28**, 438–444 (2001).
[10]J. Prince and J. Links, *Medical Imaging Signals and Systems* (Pearson Prentice Hall, 2006).
[11]J. Hubbell and S. Seltzer, "Tables of x-ray mass attenuation coefficients and mass energy-absorption coefficients from 1 kev to 20 mev for elements $z = 1$ to 92 and 48 additional substances of dosimetric interest," NISTIR 5632 (NIST, Gaithersburg, MD, 1996).
[12]*Handbook of Medical Imaging, Volume 1: Physics and Psychophysics*, edited by J. Beutel, H. Kundel, and R. van Metter (SPIE Publications, Bellingham, WA, 2009).